Co-delivery of Bee Venom Melittin and a Photosensitizer with an Organic−Inorganic Hybrid Nanocarrier for Photodynamic Therapy and Immunotherapy

Haojie Liu,[†,⊥] Yan Hu,[‡,⊥] Yajie Sun,[‡,⊥] Chao Wan,[‡] Zhanjie Zhang,[‡] Xiaomeng Dai,[‡] Zihan Lin,[†] Qianyuan He,[†] Zhe Yang,[†] Piao Huang,[†] Yuxuan Xiong,[†] Jinguo Cao,[†] Xu Chen,[†] Qi Chen,[†] Jonathan F. Lovell,[§] Zushun Xu,*[†] Honglin Jin,*[‡] and Kunyu Yang*[‡]

[†]Hubei Collaborative Innovation Center for Advanced Organic Chemical Materials, Ministry of Education Key Laboratory for the Green Preparation and Application of Functional Materials, Hubei University, Wuhan, Hubei 430062, China
[‡]Cancer Center, Union Hospital, Tongji Medical College, Huazhong University of Science and Technology, Wuhan 430022, China
[§]Department of Biomedical Engineering, University at Buffalo, State University of New York, Buffalo, New York 14260, United States

Ⓢ Supporting Information

ABSTRACT: Photodynamic therapy (PDT) is a clinical cancer treatment modality based on the induction of therapeutic reactive oxygen species (ROS), which can trigger immunogenic cell death (ICD). With the aim of simultaneously improving both PDT-mediated intracellular ROS production and ICD levels, we designed a serum albumin (SA)-coated boehmite ("B"; aluminum hydroxide oxide) organic−inorganic scaffold that could be loaded with chlorin e6 (Ce6), a photosensitizer, and a honey bee venom melittin (MLT) peptide, denoted Ce6/MLT@SAB. Ce6/MLT@SAB was anchored by a boehmite nanorod structure and exhibited particle size of approximately 180 nm. Ce6/MLT@SAB could significantly reduce hemolysis relative to that of free MLT, while providing MLT-enhanced PDT antitumor effects *in vitro*. Compared with Ce6@SAB, Ce6/MLT@SAB improved Ce6 penetration of cancer cells both *in vitro* and *in vivo*, thereby providing enhanced intracellular ROS generation with 660 nm light treatment. Following phototreatment, Ce6/MLT@SAB-treated cells displayed significantly improved levels of ICD and abilities to activate dendritic cells. In the absence of laser irradiation, multidose injection of Ce6/MLT@SAB could delay the growth of subcutaneous murine tumors by more than 60%, compared to controls. When combined with laser irradiation, a single injection and phototreatment with Ce6/MLT@SAB eradicated one-third of subcutaneous tumors in treated mice. The addition of an immune checkpoint blockade to Ce6/MLT@SAB phototreatment further augmented antitumor effects, generating increased numbers of CD4+ and CD8+ T cells in tumors with concomitant reduction of myeloid-derived suppressor cells.

KEYWORDS: photodynamic therapy, cancer immunotherapy, melittin, immunogenic cell death, immune checkpoints, anti-PD-1
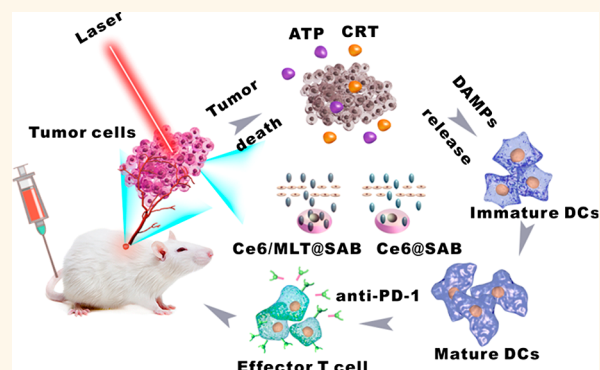
Photodynamic therapy (PDT) is a clinical cancer treatment modality that is minimally invasive, minimally toxic, and spatiotemporally selective.[1] To improve the antitumor effects of PDT, various strategies combining PDT and immune checkpoint blockades have recently been explored.[2−4] Reactive oxygen species (ROS), generated by photosensitizers during laser treatment, can directly eliminate cancer cells. Further, PDT is capable of initiating systemic antitumor immune responses by inducing the presentation of tumor-associated antigens.[5,6] Physiological barriers that surround target cells (*e.g.*, vascular walls, extracellular matrix components, and cell glycocalyx) limit the penetration of photosensitizers into tumor cells, which hampers the efficacy of PDT-mediated cancer cell killing.[7−9] Although ROS produced
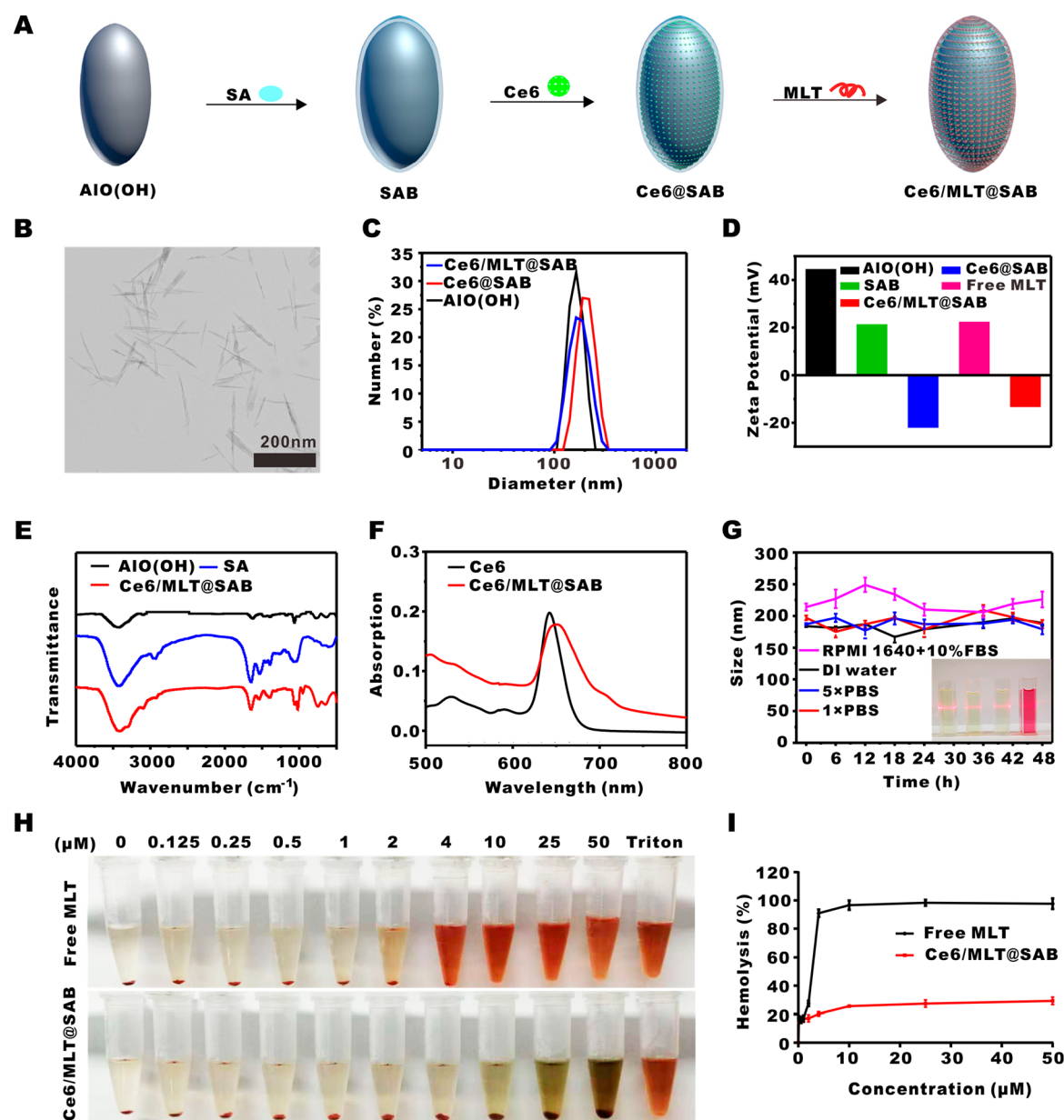
Figure 1. Characterization of Ce6/MLT@SAB. (A) Construction of Ce6/MLT@SAB. (B) TEM image of Ce6/MLT@SAB. (C) Size distributions of AlO(OH), Ce6@SAB, and Ce6/MLT@SAB. (D) Zeta-potentials at different synthetic steps. (E) FTIR spectra of AlO(OH), SA, and Ce6/MLT@SAB. (F) UV−vis spectra of Ce6/MLT@SAB and free Ce6. (G) Tyndall effect of Ce6/MLT@SAB (DI water, PBS, 5× PBS, and RPMI 1640 + 10% FBS). Data are presented as the mean ± SEM ($n = 3$). (H) Hemolysis assay of free MLT and Ce6/MLT@SAB in various solutions with MLT concentrations of 0−50 μM. (I) Relative hemolysis percentages based on treatment with free MLT and Ce6/MLT@SAB. Data are presented as the mean ± SEM ($n = 3$).

by PDT may trigger a certain level of immune responses, the level of immunogenic cell death (ICD) is usually insufficient to promote strong host adaptive immune activation.[10,11] Thus, the development of an approach that can facilitate photosensitizer penetration and enhance ICD levels would be beneficial for PDT-based cancer therapy.

Cytolytic peptides, one of the most effective types of candidate anticancer drugs, possess excellent lytic properties that endow them with inherent inhibitory activities toward cancer cells.[12] Melittin (MLT) is the main component of bee venom; it comprises a 26 amino acid amphipathic cationic peptide (GIGAVLKVLTTGLPALISWIKRKRQQ-NH2).[13,14] MLT acts as a nonselective cytolytic peptide that physically and chemically disrupts all prokaryotic and eukaryotic cell

membranes by forming transmembrane pores, thereby causing rapid cell death. Due to the high cytolytic activity of free MLT that directly kills cancer cells, diverse platforms have been developed to deliver MLT.[15−18] MLT-induced membrane permeability enhancement and cell death occur nearly simultaneously. In this context, we hypothesized that a method to reduce the toxicity of MLT could be used in membrane permeability regulation. Additionally, our previous work and a work by another group have shown that, by coupling MLT with immunological therapy, MLT-triggered cell death can enhance dendritic cell (DC) activation.[19−21] Consequently, we hypothesized that, considering the attenuated toxicity of MLT, it might facilitate the penetration of nanoparticles into the
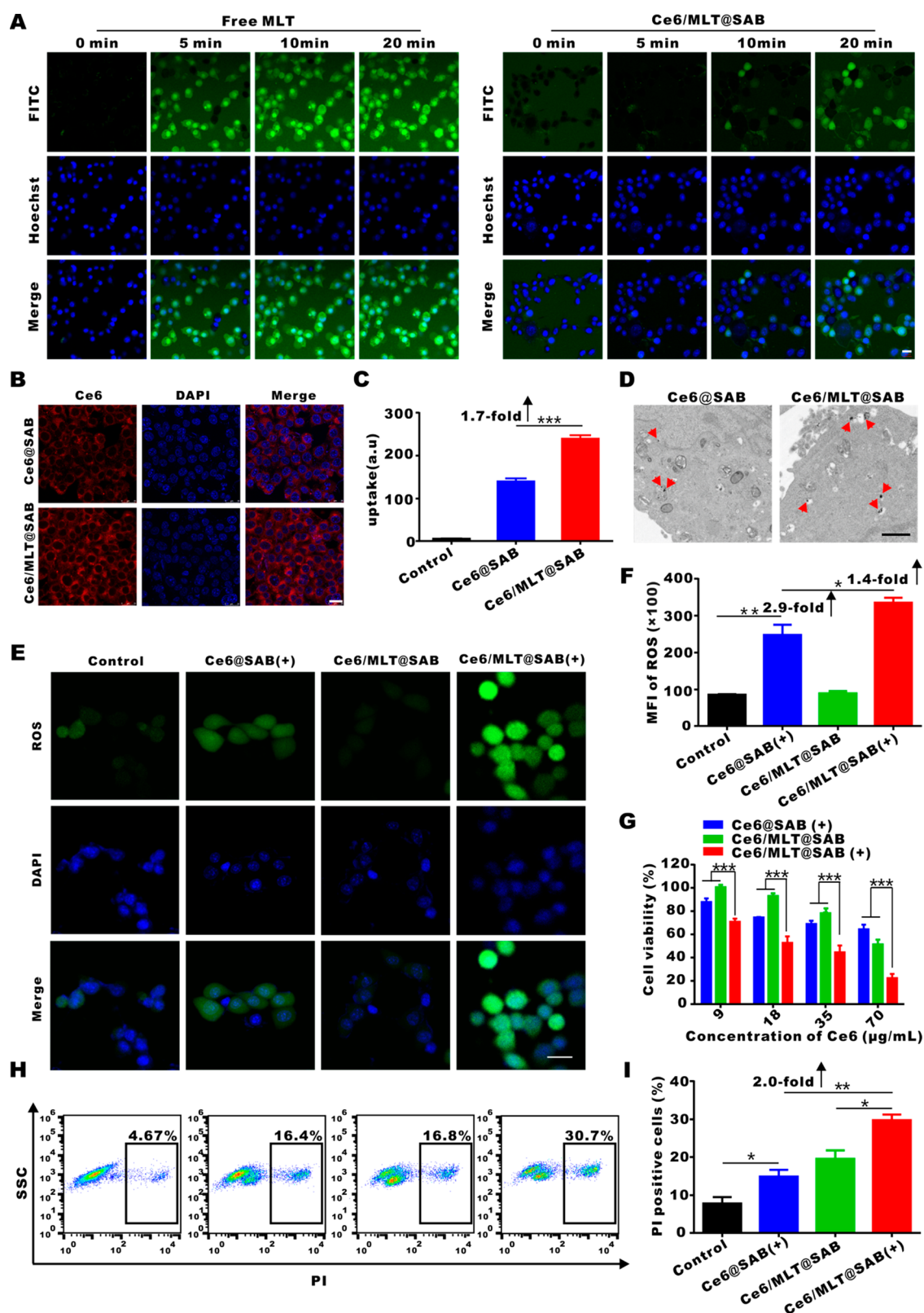
Figure 2. Cellular uptake and treatment effects of Ce6/MLT@SAB *in vitro*. (A) Confocal imaging of 4T1 cells after incubation with free MLT and FITC mixture or Ce6/MLT@SAB and FITC mixture. Scale bar = 20 μm. (B) Confocal imaging of intracellular uptake in 4T1 cells. (C) Flow cytometry quantification of Ce6 in 4T1 cells after incubation with Ce6@SAB or Ce6/MLT@SAB. Scale bar = 25 μm. (D) TEM images demonstrating intracellular uptake after incubation with Ce6@SAB and Ce6/MLT@SAB. Scale bar = 1 μm. (E) Confocal imaging of cellular ROS generation in 4T1 cancer cells. Scale bar = 50 μm. (F) Flow cytometry quantification of ROS production in 4T1 tumor cells after various treatments. (G) *In vitro* cytotoxicity of Ce6@SAB(+), Ce6/MLT@SAB, and Ce6/MLT@SAB(+) (45 s, 5 mW cm^{-2}). (H) Flow cytometry detection of apoptosis/necrosis in 4T1 cells. (I) Statistical analysis of apoptotic/necrotic 4T1 cells. The (+) indicates 660 nm laser irradiation. Data are expressed as mean $\pm$ SEM (n = 3).

tumor cells and further improve the ICD levels induced by PDT.

Herein, an organic−inorganic nanocarrier is developed with serum albumin (SA)-coated boehmite ("B", aluminum hydroxide oxide [AlO(OH)]); it is loaded with chlorin e6 (Ce6), a photosensitizer, and MLT. This construct is denoted as Ce6/MLT@SAB and is created *via* a simple and noncovalent approach. Ce6/MLT@SAB can protect against the acute toxicity of MLT and retains its ability to act on the cytomembranes of the matrix and internal organelles, thus increasing cell membrane permeability. In theory, with the assistance of MLT, the Ce6/MLT@SAB can more easily accumulate in tumor cells, permitting greater intercellular ROS production by PDT in those cells. Moreover, because of the killing effect of MLT, it can also further promote the essential ICD required for efficient antigen-presenting cell activation in the presence of combined PDT treatment. Additionally, the pro-oxidant activity of boehmite contributes to the enhanced glutathione (GSH) depletion efficiency of Ce6/MLT@SAB, which is beneficial for the tumor therapeutic effects of PDT.[22−24] Therefore, the formed platform may have the following advantages: (a) Due to the MLT-induced transmembrane pores that enhance the permeability of cancer cells, MLT can kill cancer cells effectively and can promote nanoparticle accumulation within those cells, thus promoting multiple ROS production in cancer cells. (b) With the aid of MLT, the ICD triggered by PDT achieves a more robust effect by enhancing the release of some danger-associated molecular patterns (DAMPs). Thus, this MLT synergistic immunogenic PDT nanocarrier might provide an excellent tool for boosting PDT against the tumor. (c) The nanoscale design of AlO(OH) has excellent biocompatibility with both immune and cancer cells at a high concentration; moreover, it can reduce the content of GSH, which is plentiful in the cancer cells and related to cancer progression as a result of its antioxidant and detoxification capacity, thus improving the antitumor therapeutic effect.[23,27]

RESULTS

Synthesis and Characterization of Ce6/MLT@SAB. Al compounds are considered to be nonredox active themselves but can promote biological oxidation both *in vitro* and *in vivo* as a so-called "pro-oxidant", leading to increased ROS during Al exposure. ROS subsequently can react with and deplete GSH, which is one of the most important biological antioxidants.[25−27] Therefore, we chose AlO(OH) compounds as the starting material for the synthesis of the nanoplatform. The synthetic route of the Ce6/MLT@SAB nanoplatform is shown in Figure 1A. AlO(OH) nanoparticles were synthesized by a hydrothermal method, based on previous literature.[28,29] To further improve the biocompatibility for biomedical applications, SA was incorporated into AlO(OH) nanoparticles by electrostatic interactions, resulting in SA-coated AlO(OH) nanoparticles (SAB). To synthesize Ce6/MLT@SAB, Ce6 and MLT were attached to SAB *via* electrostatic and hydrophobic interactions among Ce6, MLT, and SA, and the structures of Ce6, MLT, and SA are shown in Figure S1.[30] The shape and size of the Ce6/MLT@SAB were analyzed by transmission electron microscopy (TEM) and dynamic light scattering (DLS); Ce6/MLT@SAB has a nanorod structure with a diameter of 184.2 ± 5.4 nm, which slightly differs from those of SAB (152.4 ± 6.8 nm) and Ce6@SAB (204.9 ± 11.7 nm) (Figure 1B,C). The size difference between Ce6/MLT@SAB

and Ce6@SAB was mainly attributed to the encapsulation of MLT, owing to the positive charge of MLT which presumably allowed MLT to adsorb to Ce6@SAB (negatively charged) through electrostatic forces, which could have a contractive effect on the overall Ce6/MLT@SAB structure (Figure 1C).[31] To further investigate the physiochemical properties of the platform, zeta-potentials of AlO(OH), SAB, Ce6@SAB, free MLT, and Ce6/MLT@SAB were measured, as shown in Figure 1D. Compared to Ce6@SAB (-23.4 ± 1.5 mV), Ce6/MLT@SAB showed an increased zeta-potential of -17.6 ± 1.5 mV, suggesting successful loading of the positively charged MLT (22.5 ± 1.5 mV); this was consistent with the DLS result. The Fourier transform infrared (FTIR) spectra of AlO(OH), SA, and Ce6/MLT@SAB nanocomposites are shown in Figure 1E. The significant peaks of the characteristic stretching vibration of amide carbonyl and the bending vibration of N−H in secondary amines were detected at 1658 and 1533 cm^{-1},[32,33] and these demonstrated the presence of SA in Ce6/MLT@SAB. Additionally, Ce6 loading in Ce6/MLT@SAB was confirmed by UV−vis absorbance (Figure 1F). After Ce6 loading, the absorption of Ce6/MLT@SAB demonstrated a characteristic peak at 660 nm, which was slightly red-shifted compared to the peak of pure Ce6 (650 nm), possibly due to the interaction between Ce6 and SA. The Tyndall effect of Ce6/MLT@SAB was visibly observed; it showed no major hydrodynamic size change within 48 h (Figure 1G), thus demonstrating its excellent stability.[34] By further observing size fluctuations of the NPs in different media over a sustained period of time, it was found that Ce6/MLT@SAB was stable in deionized (DI) water, phosphate-buffered saline (PBS), and 10% fetal bovine serum (FBS) plus cell culture medium, pointing toward stability in storage and for *in vivo* applications (Figure S2). We have carried out studies to illustrate potential clinical applications of MLT.[19,35,36] As mentioned above, we found that SA could serve as an excellent stabilizer and could ensure facile MLT loading onto Ce6/MLT@SAB, with a high efficiency of 38% for MLT encapsulation (Figure S3). More importantly, the use of Ce6/MLT@SAB only resulted in 25% hemolysis with MLT concentrations up to 50 μM (Figure 1H,I), whereas the concentration of free MLT that could cause complete lysis of red blood cells (RBCs) was 4 μM, indicating that the established platform could greatly improve MLT hemocompatibility. Finally, we tested the pro-oxidant activity of Ce6/MLT@SAB and found that the nanoplatform could effectively reduce the GSH content in 4T1 cells (Figure S4). Together, these results suggested that we successfully synthesized a biocompatible, versatile, and MLT-loaded nanoplatform.

Cellular Uptake and Therapeutic Effect of Ce6/MLT@SAB *in Vitro*. In this study, we selected 4T1 cells as a model for the following experiments. Considering that MLT can disrupt plasma membranes, we mixed free MLT or Ce6/MLT@SAB with a fluorophore (FITC) solution and observed 4T1 cells by laser confocal microscopic imaging to assess membrane permeabilization. As shown in Figure 2A, most 4T1 cells treated with free MLT had been dyed by the FITC by 5 min, indicating membrane permeabilization. However, the dye remained external for the Ce6/MLT@SAB group at that time point. The dye did not start to enter into cells until 10 min, which indicates that the encapsulated MLT in Ce6/MLT@SAB was still active; after the SA binds to membranes, the MLT component may then begin to produce transmembrane pores. To assess the cellular uptake ability of Ce6/MLT@SAB
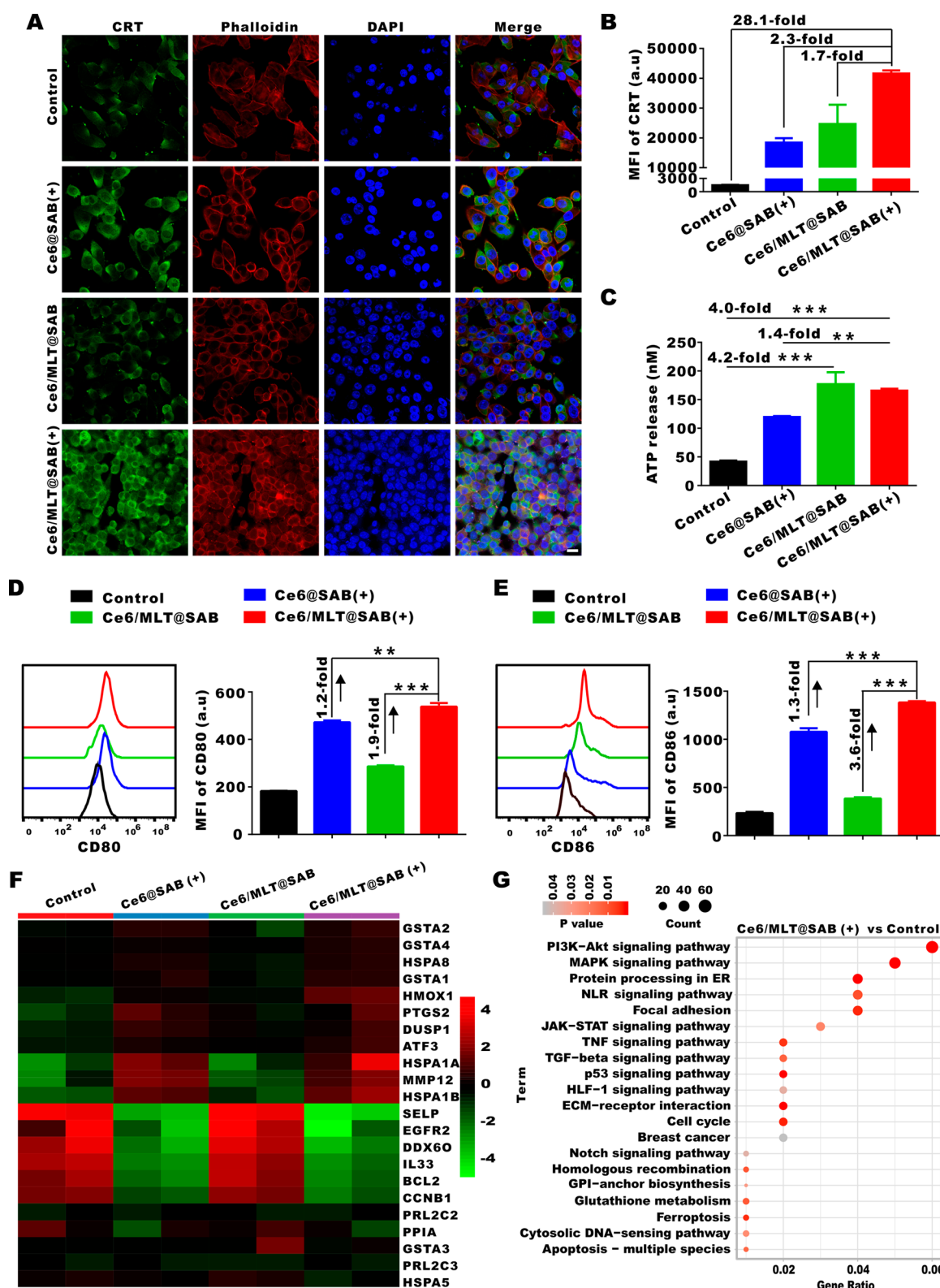
Figure 3. ICD elicited by MLT-mediated PDT *in vitro*. (A) Immunofluorescence staining of CRT expression (green) on 4T1 cell surfaces after different treatments. Phalloidin (red) represents the cytoskeleton. Scale bar = 20 μm. (B) Flow cytometric analysis of CRT expression quantification. (C) ATP release by 4T1 cells after various treatments. (D) Flow cytometric analysis of CD80 expression by mature DCs after immature DCs were stimulated with treated 4T1 cells. (E) Flow cytometric analysis of CD86 expression by mature DCs after immature DCs were stimulated with treated 4T1 cells. Data are presented as the mean ± SEM ($n = 3$). (F) Clustered analysis of differential expression of genes ($p < 0.05$). (G) KEGG pathway enrichment analysis for enriched genes treated by Ce6/MLT@SAB(+) ($p < 0.05$).

that was endowed by MLT, the cellular internalization behaviors of the nanoplatforms in the presence or absence of

MLT against 4T1 cells were compared by confocal imaging, flow cytometry, and TEM. As observed in Figure 2B,
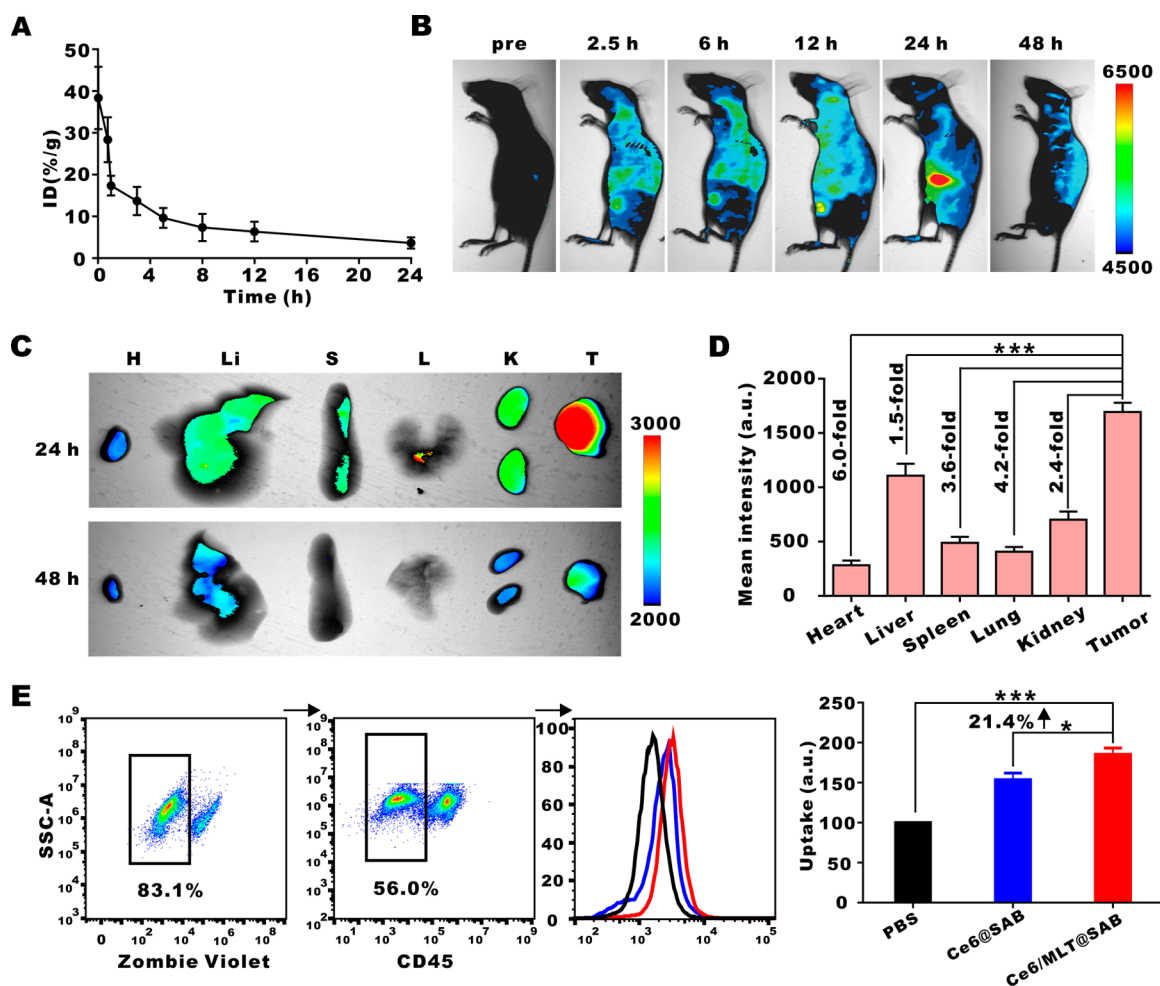
Figure 4. *In vivo* imaging and pharmacokinetics. (A) Pharmacokinetics profiles of Ce6/MLT@SAB after i.v. injection into the mice. (B) *In vivo* fluorescence images of 4T1 tumor-bearing mice after injection of Ce6/MLT@SAB. (C) *In vitro* fluorescence images of major mouse organs and tumors at 48 h after injection of Ce6/MLT@SAB. (D) Fluorescence intensities of mouse tissues as evaluated by quantitative analysis. Data are presented as the mean $\pm$ SEM ($n = 4$). (E) Tumor uptake of Ce6@SAB or Ce6/MLT@SAB, analyzed by flow cytometry. Data are presented as the mean $\pm$ SEM ($n = 5$).

compared to the platform without MLT (Ce6@SAB), Ce6/MLT@SAB-treated cells displayed much higher fluorescence signals under the same conditions, indicating increased capture of nanoplatform-carried Ce6. Moreover, flow cytometry analysis showed that the uptake of Ce6/MLT@SAB by 4T1 cells was 1.7-fold higher than that of Ce6@SAB (Figure 2C). In addition, TEM images showed that the 4T1 cells treated with Ce6/MLT@SAB had better intercellular accumulation and showed a pattern that was more likely to be cytoplasmic distribution; in contrast, endosomal/lysosomal distribution was dominant for Ce6@SAB-treated cells (Figure 2D). Indeed, the cytoplasmic distribution of photosensitizers is often thought to be superior to endosomal/lysosomal distribution with respect to PDT efficacy.[37−39] These results indicated that MLT loading facilitated the uptake and altered the cellular distribution patterns of Ce6/MLT@SAB. It is well-known that the intercellular internalization of nanoparticles often involves one or more endocytosis pathways, wherein MLT can form transmembrane pores through breakage of cell membranes.[40] However, according to the findings of previous studies, MLT treatment can lead to rapid cell death upon formation of transmembrane pores due to the high cytolytic activity of free MLT. Notably, in this study, we verified that MLT loading

onto the Ce6@SAB platform quenched MLT toxicity and increased cell permeability without causing rapid and extensive cell death, thus leading to enhanced cellular uptake.

The therapeutic effect of PDT is known to be largely dependent on the generation of ROS, which can kill cancer cells. To assess the ROS level produced by Ce6/MLT@SAB solution under laser irradiation, measurements were performed by using an ROS probe (3-diphenylisobenzofuran [DPBF]).[41,42] Figure S5 shows that Ce6/MLT@SAB and Ce6@SAB had extremely similar decay curves with respect to DPBF absorbance; these were much slower than those of free Ce6, indicating a relative decrease in the level of ROS production. Moreover, confocal imaging and flow cytometry with a classical ROS probe (DCFH-DA) were conducted to verify these conclusions in 4T1 cells. As shown in Figure 2E, cells that received Ce6/MLT@SAB and 660 nm light treatment, denoted as Ce6/MLT@SAB(+), showed the strongest green fluorescence signal compared with that of the control, Ce6@SAB(+), and Ce6/MLT@SAB groups; this confirmed significantly enhanced ROS generation. Similarly, flow cytometry analysis further demonstrated that Ce6/MLT@SAB(+)-treated cells exhibited ROS production significantly higher than that observed in any other groups
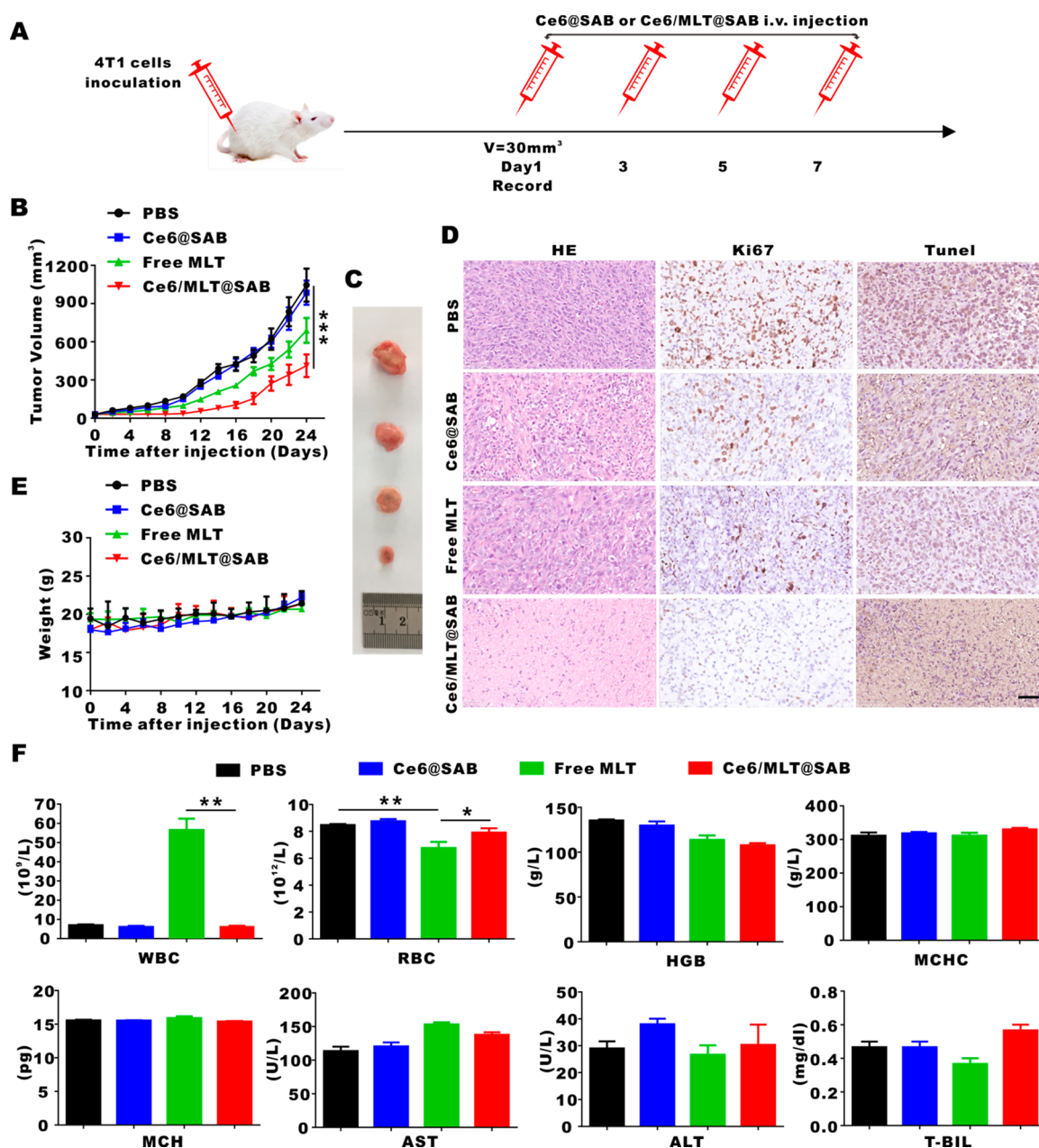
Figure 5. *In vivo* evaluation of the platforms' antitumor effects and systemic toxicity. (A) Schematic illustration of the experimental approach of Ce6/MLT@SAB. (B) Growth curves of tumors with various treatments. (C) Representative tumors in each group. (D) Hematoxylin and eosin staining, Ki67, and TUNEL immunohistochemical staining of tumors from groups that received various treatments. Scale bar = 50 μm. (E) Body weights in mice after various treatments. Data are presented as the mean $\pm$ SEM ($n = 6$) for (B,E). (F) Hemanalysis of WBC count, RBC count, HGB, MCHC, MCH, AST, ALT, and T-Bil. Data are presented as the mean $\pm$ SEM ($n = 3$).

(Figure 2F). As Ce6/MLT@SAB integrated the functions of both MLT and Ce6@SAB, the antitumor effects of MLT-based tumor therapy and Ce6-based phototreatment were then studied using cell counting kit-8 assay (CCK-8). As shown in Figure 2G, Ce6/MLT@SAB(+)-treated cells displayed the greatest killing effects, compared to Ce6@SAB(+) and Ce6/MLT@SAB-treated groups, at tested concentrations ranging from 9 to 70 μg/mL. We calculated the combination index through the Chou–Talalay method and found that this combination was synergistic (Figure S6). Notably, the killing effect of the Ce6@SAB(+) group was not obvious, which is likely due to inadequate laser power or illumination time. Subsequently, the laser power was increased, and the killing effect of the group was considerably improved (Figure S7).

Finally, we explored the synergistic therapeutic effect using an *in vitro* apoptosis assay. As expected, Ce6/MLT@SAB(+) induced apoptosis/necrosis in 31% of cells, whereas Ce6@SAB(+) and Ce6/MLT@SAB induced apoptosis/necrosis in 18 and 16% of cells, respectively (Figure 2H,I). These data indicate that the synergistic therapy possessed significant lethal effects against 4T1 cells, and MLT loading onto Ce6/MLT@SAB added to the therapeutic effect of Ce6/MLT@SAB.

In Vitro ICD Elicited by MLT-Mediated PDT. ICD is generally regarded as a requirement for effective cancer immunotherapy. Many studies and considerable clinical evidence have demonstrated that PDT can elicit ICD, which involves the release of DAMPs, including calreticulin (CRT), extracellular adenosine triphosphate (ATP), and high mobility

group box 1 (HMGB1). Such signals promote the maturation of DCs, which can effectively present antigens and mobilize host adaptive immunity.[43] To verify whether MLT synergism with PDT could further promote ICD, we treated 4T1 cells with PBS, Ce6@SAB(+), Ce6/MLT@SAB, or Ce6/MLT@SAB(+), followed by measurement of CRT expression and ATP secretion. The cell-surface CRT expression was detected by confocal laser scanning microscopy (CLSM) and flow cytometry. CLSM showed that cell-surface signals (green) dramatically increased in Ce6/MLT@SAB, Ce6@SAB(+), and Ce6/MLT@SAB(+) groups (Figure 3A), compared with the signals of the control group. The Ce6/MLT@SAB(+)-treated cells showed the greatest level of cell-surface CRT expression; it was 1.7-fold, 2.3-fold, and 28.1-fold higher than the levels of expression in the Ce6/MLT@SAB, Ce6@SAB(+), and control group, respectively. Notably, cancer cells treated with Ce6/MLT@SAB also showed cell-surface CRT expression much greater than that of the control group (Figure 3B). Moreover, the Ce6/MLT@SAB(+) and Ce6/MLT@SAB groups had very similar levels of ATP secretion, which were 4.0-fold and 4.2-fold higher than those of the control group, respectively (Figure 3C). To explore whether Ce6/MLT@SAB(+) could promote DC maturation, mouse bone-marrow-derived DCs from BALB/C mice were cultured with 4T1 cells that had been subjected to various treatments. DC maturation was analyzed with the CD86 and CD80 markers by using flow cytometry. As shown in Figure 3D,E, treatment with Ce6/MLT@SAB(+) resulted in significantly enhanced percentages of CD86^{+} and CD80^{+} cells, compared with the other groups, indicating improved capacity for triggering DC maturation. Several research studies have shown that ROS can elicit ICD.[10,11,44] To assess the potential mechanism of immune activation, we performed transcriptome sequencing in 4T1 cells under different treatment conditions. The differential gene expression levels between each treated group compared to those with the control are shown in Figure S8A. Some of the enriched genes are displayed in Figure 3F and were partly verified by QT-PCR (real-time quantitative PCR) (Figure S8B). We found that the PI3K-Akt signaling pathway, which plays a role in ATP secretion and exposure of CRT on the surface of cancer cells, was strongly enriched with 660 nm laser irradiation (Figure 3G). Thus, we concluded that MLT loading played an important role in Ce6/MLT@SAB(+)-triggered ICD and in maturation of DCs, which was also verified in vivo (Figure S9).

***In Vivo* Imaging and Pharmacokinetics.** Next, we investigated the *in vivo* pharmacokinetic behavior of Ce6@SAB and Ce6/MLT@SAB using inductively coupled plasma mass spectrometry (ICP-MS). As shown in Figure S10 and Figure 4A, Ce6@SAB and Ce6/MLT@SAB, respectively, had a relatively long blood half-life of 4.6 and 3.6 h, possibly due to their ideal size (100−400 nm), which effectively enabled avoidance of clearance by the liver, spleen, and kidney.[45] Furthermore, stable surface capping of SA may have rendered them able to escape rapid phagocytosis by macrophages.[46] Ce6 molecules could serve as near-infrared (NIR) fluorescence probes; thus, *in vivo* whole-body NIR imaging was performed on 4T1-tumor-bearing mice that had been intravenously (denoted as i.v.) injected with Ce6/MLT@SAB. Typical *in vivo* NIR images are shown in Figure 4B; fluorescence intensity gradually enhanced in the tumor regions with time and reached its peak at 24 h after injection of Ce6/MLT@SAB. At 24 and 48 h, subsets of mice were sacrificed to allow harvesting of the tumors and main organs for imaging. Consistent with the *in*

vivo fluorescence imaging results, *ex vivo* images further confirmed the preferable distribution of Ce6/MLT@SAB in tumors (Figure 4C); these were 6.0-fold, 1.5-fold, 3.6-fold, 4.2-fold, and 2.4-fold higher than those observed in hearts, livers, spleens, lungs, and kidneys at 24 h postinjection (Figure 4D). Therefore, we used the interval of 24 h for the following phototherapy studies.

To increase the effectiveness of PDT treatment, the photosensitizer must be distributed in tumor cells but not in the extracellular matrix; this elevates the efficacy of ROS. Thus, the *in vivo* uptake of Ce6/MLT@SAB by tumor cells was also examined by flow cytometry at 24 h after i.v. injection of Ce6/MLT@SAB. Importantly, the Ce6/MLT@SAB-treated mice showed much higher intercellular fluorescence signals, which increased by 21.4% compared to those in Ce6@SAB-treated mice (Figure 4E). This result might be related to the ability of MLT to form transmembrane pores that improve the accumulation of Ce6/MLT@SAB in tumor cells.

***In Vivo* Anticancer Effect of Ce6/MLT@SAB.** To assess the therapeutic potential of Ce6/MLT@SAB, we performed preliminary experiments using Ce6/MLT@SAB for treatment of established subcutaneous 4T1 tumors in mice. When tumor volumes reached approximately 30 mm³, the mice received four doses of i.v. injection of PBS, Ce6@SAB, free MLT (2.5 mg/kg), or Ce6/MLT@SAB (2.5 mg/kg MLT) every 2 days (Figure 5A). As depicted in Figure 5B, similar to the PBS control, the average tumor volume in the Ce6@SAB-treated group became progressively larger with time and exceeded 1000 mm³ at 24 days post-treatment. As expected, both free MLT and Ce6/MLT@SAB-treated mice showed obvious tumor growth inhibition. The Ce6/MLT@SAB-treated group showed significantly greater inhibitory efficacy (65.3%) compared to that of the MLT group (34.6%), possibly due to the nanoplatform design that supported better blood circulating time and tumor accumulation. Representative dissected tumors of each group are shown in Figure 5C, with additional tumor images shown in Figure S11; the tumor tissues were stained with hematoxylin and eosin staining, TUNEL, and Ki67 for histological examinations. The results showed that treatment with Ce6/MLT@SAB induced an optimal level of necrotic lesions and the highest rate of apoptosis (Figure 5D). To assess the biocompatibility of these treatments, the body weights of mice from each group were measured, and blood was collected from the mice at 24 days post-treatment for biochemical analysis and hemanalysis. Throughout the experiment, mice treated with Ce6/MLT@SAB remained normal, as demonstrated by the absence of abnormal behavioral changes or body weight loss (Figure 5E). There were no notable differences in the number of RBCs, mean corpuscular hemoglobin concentration (MCHC), level of hemoglobin (HGB) and mean corpuscular hemoglobin (MCH), and the hepatic/renal functional parameters [alanine transaminase (ALT), aspartate aminotransferase (AST), and total bilirubin (T-Bil)] among the four groups (Figure 5F). However, the white blood cell (WBC) count in the free MLT group was approximately 10-fold higher than that in other groups and was not in the normal range, indicating a degree of potential systemic toxicity. With respect to the designed Ce6/MLT@SAB, there were negligible abnormalities of the major organs, implying little or no side effects (Figure S12).

Effects of Ce6/MLT@SAB-Mediated Phototreatment *in Vivo*. Next, we sought to explore the therapeutic combination effects of Ce6/MLT@SAB and phototreatment
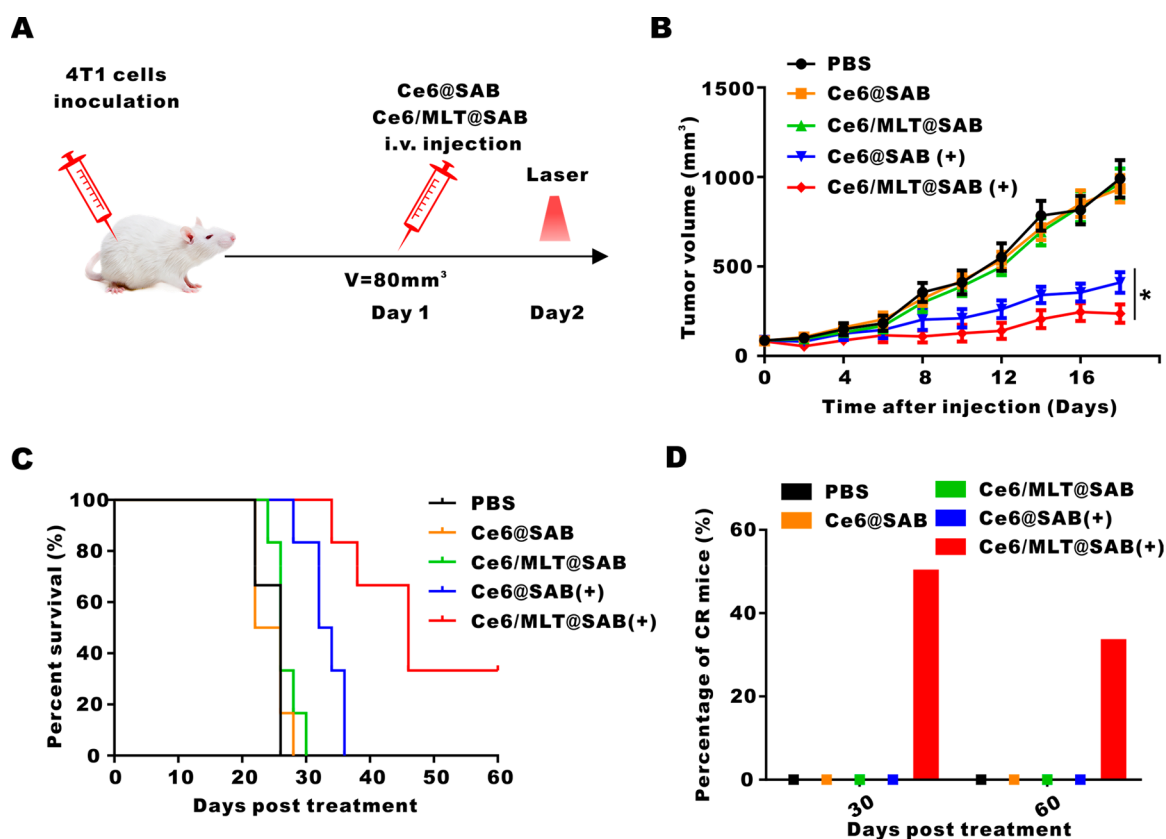
Figure 6. *In vivo* combination therapeutic effects of Ce6/MLT@SAB-mediated phototreatment. (A) Schematic illustration of MLT-mediated PDT. (B) Growth curves of tumors with disparate treatments. (C) Survival rates of mice with various treatments. (D) Percentages of CR mice in each treatment group. Data are presented as the mean $\pm$ SEM ($n = 6$) for (B−D).

(Figure 6A). When tumor volumes reached approximately 80 mm^3, each mouse received a single dose of i.v. injection of PBS, Ce6@SAB, Ce6/MLT(+), or Ce6/MLT@SAB(+). As shown in Figure 6B, at 18 days post-treatment, the average tumor volume in the control group exceeded 1000 mm^3, whereas the Ce6/MLT@SAB(+) group had an average tumor volume of 292.3 mm^3, indicating that Ce6/MLT@SAB(+) could provide strong tumor inhibition. Moreover, the inhibitory rate for Ce6/MLT@SAB(+) reached 73.5%, which was significantly higher than that of Ce6/MLT(+) (57.5%), further confirming the central role of MLT in mediating the enhanced antitumor efficacy. For this experiment, the tumor growth was recorded for 60 days. As shown in Figure 6C, the mice in PBS, Ce6@SAB, and Ce6/MLT@SAB groups were all dead (average tumor volumes >1000 mm^3). At day 35, the survival rates of mice treated with Ce6@SAB(+) and Ce6/MLT@SAB(+) were 33.3 and 83.3%, respectively. Moreover, the percentage of mice with complete regression reached 33.3% at day 60 in the Ce6/MLT@SAB(+)-treated group, but complete regression was not observed among Ce6@SAB(+)-treated mice, suggesting that Ce6/MLT@SAB(+) treatment could ablate existing tumors (Figure 6D). Overall, these data suggested that Ce6/MLT@SAB phototreatment can eliminate subcutaneous breast tumors.

Combination of Immunotherapy and Ce6/MLT@SAB Phototreatment. Due to the enhanced ICD levels mediated by Ce6/MLT@SAB(+) *in vitro*, it is imperative to explore whether Ce6/MLT@SAB phototreatment combined with anti-PD-1 immunotherapy can provide enhanced therapeutic antitumor efficacy. In this experimental setting, mice with an

average tumor volume of approximately 80 mm^3 were subjected to various treatments. In the anti-PD-1 or anti-PD-1 + Ce6/MLT@SAB phototreatment groups, mice received anti-PD-1 treatments on days 3, 5, and 7 (Figure 7A). As expected, anti-PD-1 + Ce6/MLT@SAB phototreatment demonstrated the greatest therapeutic efficacy relative to that of anti-PD-1 alone, Ce6/MLT@SAB(+), and Ce6/MLT@SAB treatments (Figure S13). An increasing body of evidence indicates that T cells play an important role in adaptive antitumor immune responses, thus we also measured the infiltration of T cells in tumors to assess the immunotherapeutic effect. The gating strategy for CD4$^+$ T cells and CD8$^+$ T cells, defined by Zom$^-$CD45$^+$CD4$^+$ and Zom$^-$CD45$^+$CD8$^+$ cells, respectively, is shown in Figure 7B. As shown in Figure 7C, the percentage of CD4$^+$ T cells in the anti-PD-1 + Ce6/MLT@SAB phototreatment group was 6.7-fold higher than that of the PBS group. Similarly, the percentage of CD8$^+$ T cells in the anti-PD-1 + Ce6/MLT@SAB phototreatment group was higher than the percentages in the PBS, Ce6@SAB(+), Ce6/MLT@SAB, and Ce6/MLT@SAB(+) groups (Figure 7D). Previous studies have demonstrated that myeloid-derived suppressor cells (MDSCs) are detrimental to cancer immunotherapy, based on the functional inhibition of CD8$^+$ T cells that facilitates tumor growth.[47−49] The gating strategy for MDSCs, defined by Zom$^-$CD45$^+$CD11b$^+$GR1$^+$ cells, is shown in Figure 7E. As shown in Figure 7F, treatments with Ce6/MLT@SAB and anti-PD-1 alone had no obvious effects on the numbers of MDSCs. As expected, the administration of the anti-PD-1 + Ce6/MLT@SAB phototreatment significantly prolonged the survival of the mice (Figure 7G). Whereas
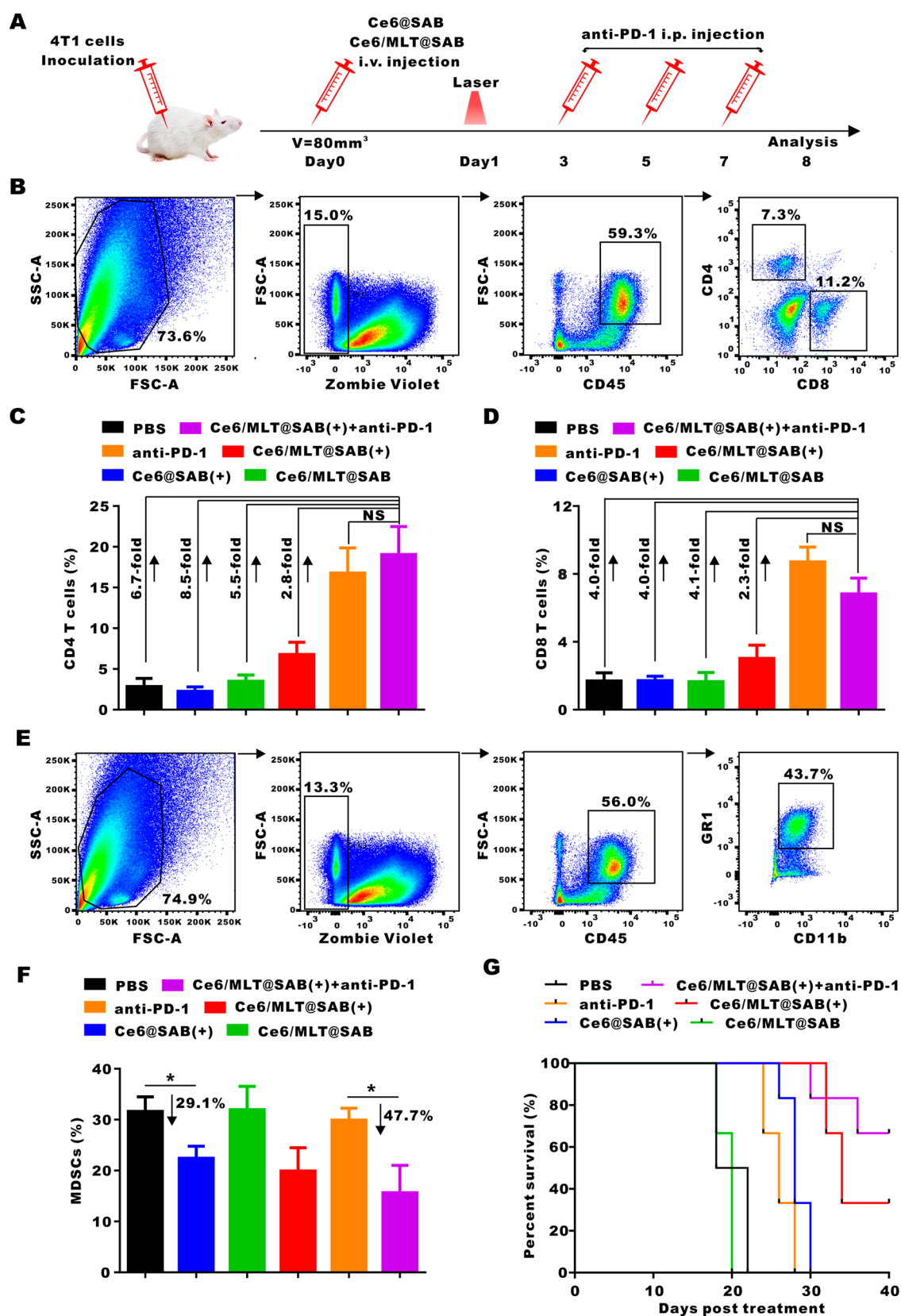
Figure 7. *In vivo* activation of immune responses elicited by MLT-mediated immunogenic PDT. (A) Schematic illustration of experimental approach of Ce6/MLT@SAB-mediated immunotherapy. (B) Gating strategy for flow cytometric analysis of T cells. (C,D) Flow cytometric analysis of the percentages of CD4$^+$ and CD8$^+$ T cells with various treatments. (E) Gating strategy for flow cytometric analysis of MDSCs. (F) Flow cytometric analysis of MDSCs in tumors with various treatments. (G) Survival rates of mice with various treatments. Data are presented as the mean $\pm$ SEM ($n = 6$) for (B–G).

treating the primary tumor with PDT can generate an adaptive immune response affecting distal tumors (abscopal effect),[50] we found out that Ce6/MLT@SAB(+) could control distal tumors more effectively with anti-PD-1 treatment (Figure S14). Collectively, our results indicated that the addition of anti-PD-1 immunotherapy can strengthen the antitumor ability of Ce6/MLT@SAB phototreatment to achieve the desired therapeutic effect.

CONCLUSION

In summary, a multifunctional platform, Ce6/MLT@SAB, was successfully created for effective delivery of MLT and Ce6. The introduction of SAB to Ce6/MLT@SAB allowed stable and efficient incorporation of MLT and greatly reduced the hemolytic effect of MLT. Based on the attenuated cytotoxicity of the carried MLT, Ce6/MLT@SAB improved Ce6 delivery into cancer cells both *in vitro* and *in vivo*, thereby promoting enhanced intracellular ROS generation with phototreatment. More importantly, Ce6/MLT@SAB-mediated phototreatment could trigger DC activation and cause high levels of ICD, thus eliciting strong antitumor immune responses. The results showed that a single injection of Ce6/MLT@SAB, combined with phototreatment, could eradicate one-third of subcutaneous tumors in a mouse model. The addition of anti-PD-1 to Ce6/MLT@SAB phototreatment further promoted these antitumor effects, resulting in increased numbers of CD4$^+$ and CD8$^+$ T cells in tumors and reduced numbers of MDSCs (Scheme 1). Thus, we have developed an organic−inorganic

Scheme 1. Depiction of an Organic−Inorganic Hybrid Nanocarrier Coloaded with Bee Venom MLT and a Photosensitizer for Combinational Photodynamic Therapy and Immunotherapy
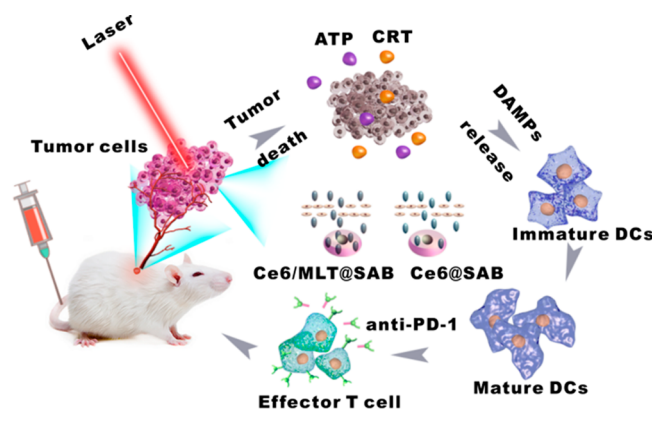
hybrid nanocarrier coloaded with bee venom MLT and a photosensitizer for combinational photodynamic therapy and immunotherapy in treatment of breast cancer.

EXPERIMENTAL SECTION

Reagents. Aluminum nitrate nonahydrate $[Al(NO_3)_3 \cdot 9H_2O]$, ethylenediamine (EDA), 1,3-DPBF, and SA were purchased from Aladdin (China). Ce6 was obtained from J&K Scientific (Beijing, China). MLT was synthesized by Bankpeptide Ltd. (Hefei, China). All chemical reagents were analytical grade and used without further purification.

Synthesis of AlO(OH) Nanoparticles. AlO(OH) nanoparticles were obtained using a previously reported method with slight modifications. Specifically, 20 mL of $[Al(NO_3)_3 \cdot 9H_2O]$ solution (69.6 mg/mL in ultrapure water) and 0.25 mL of EDA were added to a 50

mL glass vial with continuous stirring; the approximate pH of the mixture was 5. Subsequently, the mixture was transferred into a stainless-steel autoclave and maintained at 200 °C for 8 h. When the reaction was completed, the resulting AlO(OH) nanoparticles were separated by centrifugation and washed several times with ethyl alcohol and ultrapure water to remove all ionic remnants. The purified AlO(OH) nanoparticles were stored at 4 °C until use.

Synthesis of Ce6/MLT@SAB. The purified AlO(OH) nanoparticles (10 mg) were dispersed in water and mixed with SA (10 mg). Then, 1 mL of Ce6 (5 mg/mL in dimethyl sulfoxide) was added into the SA-AlO(OH) solution with vigorous mixing at room temperature in the dark. After 12 h, the resulting Ce6@SAB was purified by centrifugation and washed three times with water to remove free SA and Ce6. Subsequently, 1 mL of MLT (5 mg/mL in ultrapure water) was gradually added into the Ce6@SAB solution. Finally, the Ce6/MLT@SAB was obtained by filtering the reaction liquid with 100 kDa filters.

Instrumentation. TEM images were obtained by Tecnai G20 (FEI Corp. USA), operated at 200 kV. The zeta-potential and hydration particle size were determined by using a ZetaSizer Nano series Nano-ZS (Malvern Instruments Ltd., Malvern, UK). The chemical structure was determined by FTIR (Nicolet IS50 Thermo Fisher, USA). UV−visible absorption was measured by a UV−vis spectrophotometer (UV 1800 PC, Mapada, China). The concentration of MLT in the supernatant was measured by HPLC (SHIMADZU, Japan) at the characteristic wavelength of 214 nm and compared with the MLT standard curve. The MLT encapsulation efficiency (EE%) was calculated by using the following equation: EE% $= (W_{loaded\ drug}/W_{total\ drug}) \times 100\%$. Confocal laser scanning microscope (CLSM, Zeiss LSM 710, Germany) was used in this study.

Cell Culture. 4T1 murine breast tumor cells were purchased from American Type Culture Collection and maintained in Roswell Park Memorial Institute (RPMI) 1640 medium (Gibico) with 10% FBS (Gibico), 100 μg/mL penicillin, and 100 μg/mL streptomycin at 37 °C in an atmosphere of 5% CO_2.

Hemolysis Assay. Fresh mouse blood was collected for RBC isolation by centrifugation (1000 rpm, 5 min). RBCs were suspended at a density of 5×10^7 cells/mL in PBS buffer. For the hemolysis assay, 500 μL of RBCs was incubated with various concentrations of free MLT and Ce6/MLT@SAB at 37 °C for 4 h. The negative control was RBCs suspended in PBS without any treatment. The positive control was RBCs treated with 1% Triton X-100. After centrifugation (1000 rpm, 10 min), the supernatants of each group were analyzed by a microplate reader (Tecan Group Ltd., Mannedorf, Switzerland).

Intracellular ROS Measurement. For flow cytometry, 4T1 cells (4×10^4 cells/well) were seeded into 48-well plates (NSET, China) with 500 μL of RPMI 1640 medium per well and then cultured for 24 h. After this, the cells were then mixed with PBS, Ce6@SAB, or Ce6/MLT@SAB at the same concentration of Ce6 (30 μg/mL). After 4 h of incubation, the cells were irradiated with or without a 660 nm laser for 45 s (5 mW/cm^2) and then stained with DCFH-DA (Beyotime Biotechnology, China) for 0.5 h at 37 °C in an atmosphere of 5% CO_2. Finally, the cells were collected, and ROS generation was detected by flow cytometry.

For CLSM observation, cancer cells (1×10^4 cells/well) were seeded into 24-well plates (NSET, China) with 1 mL of RPMI 1640 medium per well and cultured for 24 h. 4T1 Cells were then treated with PBS, Ce6@SAB, or Ce6/MLT@SAB at the identical amount of Ce6 (30 μg/mL). After being incubated for 4 h, the cells were treated with or without a 660 nm laser for 45 s (5 mW/cm^2) and then stained with DCFH-DA for 0.5 h at 37 °C in an atmosphere of 5% CO_2, followed by 1 μM 4′,6-diamidino-2-phenylindole (DAPI) staining (Invitrogen, USA) for 10 min. Finally, the cells were observed by using a fluorescence confocal microscope at an excitation wavelength of 488 nm for DCF and 405 nm for DAPI.

Cell Viability Experiment. 4T1 cells (8×10^3 cells/well) were seeded into a 96-well plate (NSET, China) and further cultured with 100 μL of medium per well for 24 h. After being treated with Ce6@SAB or Ce6/MLT@SAB at various concentrations of Ce6 and cultured for 4 h, these cells were irradiated with or without a 660 nm

laser for 45 s (5 mW/cm^2). After 24 h incubation, cell viability was determined by the CCK-8 assay (Beyotime Biotechnology, China).

Apoptosis Assay. 4T1 cells (4×10^4 cells/well) were seeded into 48-well plates with moderate medium and cultured for 24 h. After being treated with PBS, Ce6@SAB, or Ce6/MLT@SAB at an equivalent amount of Ce6 (30 μg/mL) for 4 h, the cells were irradiated with or without a 660 nm laser for 45 s (5 mW/cm^2). After incubation for 24 h, these cells were collected by trypsin without EDTA and washed with PBS. Propidium iodide (Beyotime Biotechnology, China) was added to the suspended cells for staining for 10 min; they were then analyzed by flow cytometry.

***In Vitro* Induction of DC Maturation.** BMDCs were isolated from femurs and tibiae of female BALB/c mice (6−8 weeks of age). After the removal of RBCs using RBC lysis buffer, BMDCs were cultured in RPMI 1640 medium containing 10% FBS and 20 ng/mL GM-CSF (PeproTech, USA) for 5 days. On day 6, non-adherent cells were co-incubated with 4T1 cells treated with PBS, Ce6@SAB, or Ce6/MLT@SAB at an equal concentration of Ce6 (30 μg/mL) and irradiated with or without a 660 nm laser for 45 s (5 mW/cm^2). After 24 h, DCs were stained with PE-anti-mouse CD80 and APC anti-mouse CD86 antibodies (Biolegend, USA) and then analyzed by flow cytometry.

***In Vitro* Detection of Crucial ICD Biomarkers.** Cell surface expression of CRT was detected by immunofluorescence and flow cytometry. For CLSM observation, tumor cells were seeded into 24-well plates (1×10^4 cells/well), cultured with 1 mL of RPMI 1640 medium per well for 24 h. These cells were then treated with PBS, Ce6@SAB, or Ce6/MLT@SAB at an equal amount of Ce6 (30 μg/mL) for 4 h incubation. After being irradiated with or without a 660 nm laser for 45 s (5 mW/cm^2), these cells were incubated for an additional 24 h. Then the cells were fixed with paraformaldehyde for 15 min and stained with anticalreticulin antibody (Abcam, USA) for 1 h; they were then labeled with Alexa Fluor 488-conjugated secondary antibody (Life Technologies, USA) for 1 h. After the cells were stained with phalloidin (Servicebio, China) for 1 h and DAPI for 10 min, they were observed by fluorescence CLSM (Zeiss LSM 710) at excitation wavelengths of 488 nm for CRT, 570 nm for phalloidin, and 405 nm for DAPI. For flow cytometry, 4T1 tumor cells (4×10^4 cells/well) were seeded into a 48-well plate with 500 μL of RPMI 1640 medium per well. After being cultured for 24 h, cells were added with PBS, Ce6@SAB, or Ce6/MLT@SAB at the same amount of Ce6 (30 μg/mL). After an additional 4 h incubation, the cells were irradiated with or without a 660 nm laser for 45 s (5 mW/cm^2). Twenty-four hours later, they were then stained with an anticalreticulin antibody for 30 min, followed by labeling with an Alexa Fluor 488-conjugated secondary antibody for 30 min. Finally, the cells were collected, and CRT expression was measured by flow cytometry.

Extracellularly released ATP was examined using the chemiluminescence ATP determination kit. 4T1 cells were seeded into a 96-well plate (8×10^3 cells/well) with 100 μL of RPMI 1640 medium per well. Twenty-four hours later, the cells were then incubated with Ce6@SAB or Ce6/MLT@SAB at an equivalent concentration of Ce6 (30 μg/mL) for 4 h and irradiated with or without a 660 nm laser for 45 s (5 mW/cm^2). After an additional 24 h incubation, the cell supernatant was collected and detected by the chemiluminescence ATP determination kit, in accordance with the manufacturer's protocol.

RNA-Seq Analysis. For RNA-Seq analysis, 4T1 murine breast tumor cells (4×10^4 cells/well) were seeded into 48-well plates added with 500 μL of RPMI 1640 medium per well and cultured for 24 h. 4T1 cells were then treated with PBS, Ce6@SAB, or Ce6/MLT@SAB at an identical concentration of Ce6 (30 μg/mL). Four hours later, these cells were irradiated with or without a 660 nm laser for 45 s (5 mW/cm^2). After 24 h culture, RNA of the cells was collected according to the instruction manual of the TRIzol reagent. RNA concentration and purity was measured by a NanoDrop2000 spectrophotometer (Thermo Fisher, USA) and Labchip GX Touch HT nucleic acid analyzer (PerkinElmer, USA). High-quality RNA was sent to WuHan Bioacme Biological Technologies Corporation

(Wuhan, China) for cDNA library construction and sequencing. mRNA was then enriched by oligo (dT) beads. RNA sequencing libraries were generated using the KAPA stranded RNA-Seq kit for illumina with multiplexing primers, according to the manufacturer's protocol. Then sequencing was performed on illumina Nova sequencer.

Real-Time Quantitative PCR. 4T1 cells (4×10^4 cells/well) were seeded into 48-well plates with 500 μL of RPMI 1640 medium per well and then cultured for 24 h. Cells were then treated with PBS, Ce6@SAB, or Ce6/MLT@SAB at an equal concentration of Ce6 (30 μg/mL). After 4 h of incubation, the cells were irradiated with or without a 660 nm laser for 45 s (5 mW/cm^2). After incubation for 24 h, total RNA of these treated cells was extracted with a MicroElute total RNA kit R6831-01 (OMEGA) and reversed-transcribed into cDNA using a ReverTra Ace qPCR RT kit FSQ-101 (TOYOBO, Japan). The cDNA was amplified utilizing the AceQ Universal SYBR qPCR Master Mix (Vazyme Biotech, China) on a Bio-Rad real-time PCR system (Bio-Rad, USA). The gene mRNA levels were normalized by GAPDH. The primer sequences are shown as follows: MMP12 (GCCATCTGGGCCAAAGATACC, AGTTGCTT-CTAGCCCAAAGAAC), HSPA8 (TCTCGGCACCACCTACTCC, CTACGCCCGATCAGACGTTT), ATF3 (GAGGATT-TTGCTAACCTGACACC, TTGACGGTAACTGACTCCAGC), PTGS2 (TTCAACACACTCTATCACTGGC, AGAAGCG-TTTGCGGTACTCAT), and GSTA3 (TGGCGGGGAAGC-CAGTCCTT, ACCTTGCCAGGTCATCCCGAGT). All primers were synthesized by Sangon Biotech (Shanghai) Co., Ltd.

Animal Model. Female BALB/c mice (6−8 weeks old) were purchased from HBCDC (Wuhan, China). All animal studies were performed in compliance with protocols that were approved by the Hubei Provincial Animal Care and Use Committee, following the experimental guidelines of the Animal Experimentation Ethics Committee of the Huazhong University of Science and Technology (HUST, Wuhan, China). A subcutaneous tumor model was established by subcutaneously injecting 4T1 cells (1×10^6 cells/mouse) into the right flank of each mouse. The tumor volume was enumerated using the following formula: width$^2 \times$ length $\times$ 0.5.

***In Vivo* Imaging System.** When tumor volumes reached 200 mm^3, female BALB/c mice were separated into three groups at random. A volume of 300 μL of Ce6/MLT@SAB was intravenously injected with an equal MLT concentration (2.5 mg/kg). At 2.5, 6, 12, 24, and 48 h after injection, the FL signals of Ce6 were measured by a Spectral Instruments imaging optical imaging platform (Lago X, Cold Spring Biotech Corp) (ex: 690 nm; filter: 710 nm). Tumors and major organs were also collected and imaged 24 and 48 h later.

***In Vivo* Cellular Uptake.** To explore the *in vivo* cellular uptake of the platforms, when tumor volumes reached 30 mm^3, female BALB/c mice were separated into three groups at random for various treatments (n = 5 *per* group): (1) i.v. injection with 300 μL of PBS; (2) i.v. injection with 300 μL of Ce6@SAB (Ce6 dose: 5 mg/kg); (3) i.v. injection with 300 μL of Ce6/MLT@SAB (Ce6 dose: 5 mg/kg). At 24 h after injection, these mice were sacrificed and tumors were harvested, digested, and ground to produce single-cell suspensions. These suspensions were labeled with mixtures of anti-mouse APC-A750-Zombie NIR and PE-Cy7 anti-mouse CD45 (Biolegend, USA) to identify tumor cells and then assessed by flow cytometry.

Therapeutic Effect in Animals. To explore the MLT therapeutic effect of the platforms, when tumor volumes reached 30 mm^3, female BALB/c mice were separated into four groups at random for various treatments (n = 6 per group): (1) i.v. injection with 300 μL of PBS; (2) i.v. injection with 300 μL of Ce6@SAB (Ce6 dose: 5 mg/kg); (3) i.v. injection with 300 μL of Ce6/MLT@SAB (Ce6 dose: 5 mg/kg); or (4) i.v. injection with 300 μL of free MLT (identical dose to that in Ce6/MLT@SAB, 2.5 mg/kg), every other day for a total of four doses. The body weight and tumor size of each mouse were monitored every other day for 24 days.

These mice were sacrificed at 24 days postinjection, and their major organs (hearts, livers, spleens, lungs, and kidneys) and tumor tissues were harvested for hematoxylin and eosin staining. In addition, tumors were stained with Ki67 (CST) and TUNEL (Roche) for

immunohistochemical analysis. Fresh blood of the treated animals was also harvested for biochemical analyses.

To investigate the combination effect of MLT synergism with PDT, when tumor volumes reached 80 mm³, female BALB/c mice were separated into five groups at random ($n = 6$ per group): (1) i.v. injection with 300 μL of PBS; (2) i.v. injection with 300 μL of Ce6@ SAB (Ce6 dose: 5 mg/kg); (3) i.v. injection with 300 μL of Ce6/ MLT@SAB (Ce6 dose: 5 mg/kg; MLT dose: 2.5 mg/kg); (4) i.v. injection with 300 μL of Ce6@SAB (Ce6 dose: 5 mg/kg) with a 660 nm light (0.1 W/cm², 20 min); and (5) i.v. injection with 300 μL of Ce6/MLT@SAB (Ce6 dose: 5 mg/kg; MLT dose: 2.5 mg/kg) with a 660 nm light (0.1 W/cm², 20 min).

In Vivo Antitumor Immunity. To explore antitumor immunity, when tumor volumes reached 80 mm³, female BALB/c mice were separated into six groups at random ($n = 6$ per group): (1) i.v. injection with PBS; (2) i.v. injection with Ce6@SAB with laser irradiation (Ce6 dose: 5 mg/kg); (3) i.v. injection with Ce6/MLT@ SAB (Ce6 dose: 5 mg/kg; MLT dose: 2.5 mg/kg); (4) i.v. injection with Ce6/MLT@SAB (Ce6 dose: 5 mg/kg; MLT dose: 2.5 mg/kg) with a 660 nm light (0.1 W/cm², 20 min); (5) intraperitoneal injection with anti-PD-1 (10 mg/kg every other day for a total of four doses after phototreatment); and (6) i.v. injection with Ce6/MLT@ SAB + intraperitoneal injection with anti-PD-1 (every other day for a total of four doses after phototreatment) with a 660 nm light (0.1 W/ cm², 20 min) (Ce6 dose: 5 mg/kg; MLT dose: 2.5 mg/kg; anti-PD-1 dose: 10 mg/kg). The tumor size of each mouse was monitored every other day for 9 days.

For analysis of antitumor immune responses, tumors were harvested, digested, and ground to produce single-cell suspensions. These suspensions were labeled with mixtures of anti-mouse APC-A750-Zombie NIR, PE-Cy7 anti-mouse CD45, FITC anti-mouse CD8, and PE anti-mouse CD4 to identify the T lymphocytes; or with APC-A750-Zombie NIR, PE-Cy7 anti-mouse CD45, FITC anti-mouse CD11b, and APC anti-mouse GR1 (Biolegend) to identify MDSCs. All mixtures were assessed by flow cytometry.

Statistical Analysis. Data in this study are presented as mean ± standard error of the mean (SEM). For *in vitro* studies, unpaired Students t tests were used for statistical comparison. Overall survival was analyzed using the Kaplan−Meier method. Statistical significance was expressed as * for $p < 0.05$, ** for $p < 0.01$, and *** for $p < 0.001$.

ASSOCIATED CONTENT

ⓢ Supporting Information

The Supporting Information is available free of charge on the ACS Publications website at DOI: 10.1021/acsnano.9b04181.

> Structure of Ce6, MLT, SA, and long-term hydro-dynamic stability of Ce6/MLT@SAB, efficiency of MLT encapsulation with different mass ratios of serum albumin ("SA") to MLT, intracellular GSH depletion after incubation with Ce6/MLT@SAB, DPBF absorbance decay curves of free Ce6, Ce6@SAB, and Ce6/ MLT@SAB, combination index of MLT-based tumor therapy and Ce6-based phototreatment, cell viability of 4T1 cells treated with different concentrations of Ce6@ SAB with laser irradiation, summary of genes showing altered expression and QT-PCR verification, flow cytometric analysis of CD80 and CD86 expression by mature DCs *in vivo* pharmacokinetics profiles of Ce6@ SAB after i.v. injection into the mice, photograph of dissected tumor samples in different groups as indicated, hematoxylin and eosin staining analysis of mice tissues including heart, liver, spleen, lung, and kidney from mice, tumor growth curves for mice with various treatments, abscopal effect of Ce6/MLT@SAB(+) and anti-PD-1 combining therapy (PDF)

AUTHOR INFORMATION

Corresponding Authors
*E-mail: zushunxu@hubu.edu.cn.
*E-mail: jin@hust.edu.cn.
*E-mail: yangkunyu@medmail.com.cn.

ORCID ⬡
Jonathan F. Lovell: 0000-0002-9052-884X
Zushun Xu: 0000-0001-7314-170X
Honglin Jin: 0000-0002-4398-9539

Author Contributions
[⊥]H.L., Y.H., and Y.S. contributed equally.

Notes
The authors declare no competing financial interest.

REFERENCES

(1) Dolmans, D. E.J.G.J.; Fukumura, D.; Jain, R. K. Photodynamic Therapy for Cancer. *Nat. Rev. Cancer* **2003**, *3*, 380−387.

(2) Xu, J.; Xu, L.; Wang, C.; Yang, R.; Zhuang, Q.; Han, X.; Dong, Z.; Zhu, W.; Peng, R.; Liu, Z. Near-Infrared-Triggered Photodynamic Therapy with Multitasking Upconversion Nanoparticles in Combination with Checkpoint Blockade for Immunotherapy of Colorectal Cancer. *ACS Nano* **2017**, *11*, 4463−4474.

(3) Duan, X.; Chan, C.; Guo, N.; Han, W.; Weichselbaum, R. R.; Lin, W. Photodynamic Therapy Mediated by Nontoxic Core-Shell Nanoparticles Synergizes with Immune Checkpoint Blockade to Elicit Antitumor Immunity and Antimetastatic Effect on Breast Cancer. *J. Am. Chem. Soc.* **2016**, *138*, 16686−16695.

(4) Lu, K.; He, C.; Guo, N.; Chan, C.; Ni, K.; Weichselbaum, R. R.; Lin, W. Chlorin-Based Nanoscale Metal-Organic Framework Systemically Rejects Colorectal Cancers *via* Synergistic Photodynamic Therapy and Checkpoint Blockade Immunotherapy. *J. Am. Chem. Soc.* **2016**, *138*, 12502−12510.

(5) He, C.; Duan, X.; Guo, N.; Chan, C.; Poon, C.; Weichselbaum, R. R.; Lin, W. Core-Shell Nanoscale Coordination Polymers Combine Chemotherapy and Photodynamic Therapy to Potentiate Checkpoint Blockade Cancer Immunotherapy. *Nat. Commun.* **2016**, *7*, 12499.

(6) Yang, G.; Xu, L.; Chao, Y.; Xu, J.; Sun, X.; Wu, Y.; Peng, R.; Liu, Z. Hollow MnO$_2$ As a Tumor-Microenvironment-Responsive Biodegradable Nano-Platform for Combination Therapy Favoring Antitumor Immune Responses. *Nat. Commun.* **2017**, *8*, 902.

(7) Fang, J.; Nakamura, H.; Maeda, H. The EPR Effect: Unique Features of Tumor Blood Vessels for Drug Delivery, Factors Involved, and Limitations and Augmentation of the Effect. *Adv. Drug Delivery Rev.* **2011**, *63*, 136−151.

(8) Derycke, A. S.; de Witte, P. A. Liposomes for Photodynamic Therapy. *Adv. Drug Delivery Rev.* **2004**, *56*, 17−30.

(9) Xu, Y.; Liang, X.; Bhattarai, P.; Sun, Y.; Zhou, Y.; Wang, S.; Chen, W.; Ge, H.; Wang, J.; Cui, L.; Dai, Z. Enhancing Therapeutic Efficacy of Combined Cancer Phototherapy by Ultrasound-Mediated *In Situ* Conversion of Near-Infrared Cyanine/Porphyrin Microbubbles into Nanoparticles. *Adv. Funct. Mater.* **2017**, *27*, 1704096.

(10) Castano, A. P.; Mroz, P.; Hamblin, M. R. Photodynamic Therapy and Anti-Tumour Immunity. *Nat. Rev. Cancer* **2006**, *6*, 535−545.

(11) Castano, A. P.; Mroz, P.; Wu, M. X.; Hamblin, M. R. Photodynamic Therapy plus Low-Dose Cyclophosphamide Generates

Antitumor Immunity in a Mouse Model. *Proc. Natl. Acad. Sci. U. S. A.* **2008**, *105*, 5495−5500.

(12) Papo, N.; Shai, Y. Host Defense Peptides As New Weapons in Cancer Treatment. *Cell. Mol. Life Sci.* **2005**, *62*, 784−790.

(13) Gajski, G.; Garaj-Vrhovac. Melittin: A Lytic Peptide with Anticancer Properties. *Environ. Toxicol. Pharmacol.* **2013**, *36*, 697−705.

(14) Raghuraman, H.; Chattopadhyay, A. Melittin: A Membrane-Active Peptide with Diverse Functions. *Biosci. Rep.* **2007**, *27*, 189−223.

(15) He, B.; Tan, T.; Wang, H.; Hu, H.; Wang, Z.; Wang, J.; Li, J.; Sun, K.; Zhang, Z.; Li, Y. Rational Design of Tumor Microenvironment-Activated Micelles for Programed Targeting of Breast Cancer Metastasis. *Adv. Funct. Mater.* **2018**, *28*, 1705622.

(16) Gao, J.; Xie, C.; Zhang, M.; Wei, X.; Yan, Z.; Ren, Y.; Ying, M.; Lu, W. RGD-Modified Lipid Disks As Drug Carriers for Tumor Targeted Drug Delivery. *Nanoscale* **2016**, *8*, 7209−7216.

(17) Zetterberg, M. M.; Reijmar, K.; Pranting, M.; Engstrom, A.; Andersson, D. I.; Edwards, K. PEG-Stabilized Lipid Disks As Carriers for Amphiphilic Antimicrobial Peptides. *J. Controlled Release* **2011**, *156*, 323−328.

(18) Oude Blenke, E.; Sleszynska, M.; Evers, M. J.; Storm, G.; Martin, N. I.; Mastrobattista, E. Strategies for the Activation and Release of the Membranolytic Peptide Melittin from Liposomes Using Endosomal pH As a Trigger. *Bioconjugate Chem.* **2017**, *28*, 574−582.

(19) Jin, H.; Wan, C.; Zou, Z.; Zhao, G.; Zhang, L.; Geng, Y.; Chen, T.; Huang, A.; Jiang, F.; Feng, J. P.; Lovell, J. F.; Chen, J.; Wu, G.; Yang, K. Tumor Ablation and Therapeutic Immunity Induction by an Injectable Peptide Hydrogel. *ACS Nano* **2018**, *12*, 3295−3310.

(20) Lee, C.; Bae, S. S.; Joo, H.; Bae, H. Melittin Suppresses Tumor Progression by Regulating Tumor-Associated Macrophages in a Lewis Lung Carcinoma Mouse Model. *Oncotarget* **2017**, *8*, 54951−54965.

(21) Hwang, D. S.; Kim, S. K.; Bae, H. Therapeutic Effects of Bee Venom on Immunological and Neurological Diseases. *Toxins* **2015**, *7*, 2413−2421.

(22) Wang, S.; Li, F.; Qiao, R.; Hu, X.; Liao, H.; Chen, L.; Wu, J.; Wu, H.; Zhao, M.; Liu, J.; Chen, R.; Ma, X.; Kim, D.; Sun, J.; Davis, T. P.; Chen, C.; Tian, J.; Hyeon, T.; Ling, D. Arginine-Rich Manganese Silicate Nanobubbles As a Ferroptosis-Inducing Agent for Tumor-Targeted Theranostics. *ACS Nano* **2018**, *12*, 12380−12392.

(23) Deng, Y.; Jia, F.; Chen, S.; Shen, Z.; Jin, Q.; Fu, G.; Ji, J. Nitric Oxide As an All-Rounder for Enhanced Photodynamic Therapy: Hypoxia Relief, Glutathione Depletion and Reactive Nitrogen Species Generation. *Biomaterials* **2018**, *187*, 55−65.

(24) Zhang, H.; Liu, K.; Li, S.; Xin, X.; Yuan, S.; Ma, G.; Yan, X. Self-Assembled Minimalist Multifunctional Theranostic Nanoplatform for Magnetic Resonance Imaging-Guided Tumor Photodynamic Therapy. *ACS Nano* **2018**, *12*, 8266−8276.

(25) Yousef, M. I.; Salama, A. F. Propolis Protection from Reproductive Toxicity Caused by Aluminium Chloride in Male Rats. *Food Chem. Toxicol.* **2009**, *47*, 1168−1175.

(26) Gomez, M.; Esparza, J. L.; Nogues, M. R.; Giralt, M.; Cabre, M.; Domingo, J. L. Pro-Oxidant Activity of Aluminum in the Rat Hippocampus: Gene Expression of Antioxidant Enzymes After Melatonin Administration. *Free Radical Biol. Med.* **2005**, *38*, 104−111.

(27) Murakami, K.; Yoshino, M. Aluminum Decreases the Glutathione Regeneration by the Inhibition of NADP-Isocitrate Dehydrogenase in Mitochondria. *J. Cell. Biochem.* **2004**, *93*, 1267−1271.

(28) Chen, X. Y.; Lee, S. W. pH-Dependent Formation of Boehmite (γ-AlOOH) Nanorods and Nanoflakes. *Chem. Phys. Lett.* **2007**, *438*, 279−284.

(29) Sun, B.; Ji, Z.; Liao, Y.-P.; Wang, M.; Wang, X.; Dong, J.; Chang, C. H.; Li, R.; Zhang, H.; Nel, A. E.; Xia, T. Engineering an Effective Immune Adjuvant by Designed Control of Shape and Crystallinity of Aluminum Oxyhydroxide Nanoparticles. *ACS Nano* **2013**, *7*, 10834−10849.

(30) Bourassa, P.; Kanakis, C. D.; Tarantilis, P.; Pollissiou, M. G.; Tajmir-Riahi, H. A. Resveratrol, Genistein, and Curcumin Bind Bovine Serum Albumin. *J. Phys. Chem. B* **2010**, *114*, 3348−3354.

(31) Huang, B. X.; Kim, H. Y.; Dass, C. Probing Three-Dimensional Structure of Bovine Serum Albumin by Chemical Cross-Linking and Mass Spectrometry. *J. Am. Soc. Mass Spectrom.* **2004**, *15*, 1237−1247.

(32) Hu, Y. J.; Liu, Y.; Sun, T. Q.; Bai, A. M.; Lu, J. Q.; Pi, Z. B. Binding of Anti-Inflammatory Drug Cromolyn Sodium to Bovine Serum Albumin. *Int. J. Biol. Macromol.* **2006**, *39*, 280−285.

(33) Hu, Y. J.; Liu, Y.; Zhang, L. X.; Zhao, R. M.; Qu, S. S. Studies of Interaction between Colchicine and Bovine Serum Albumin by Fluorescence Quenching Method. *J. Mol. Struct.* **2005**, *750*, 174−178.

(34) Yoon, Y.-s.; Lee, B.-I.; Lee, K. S.; Im, G. H.; Byeon, S.-H.; Lee, J. H.; Lee, I. S. Surface Modification of Exfoliated Layered Gadolinium Hydroxide for the Development of Multimodal Contrast Agents for MRI and Fluorescence Imaging. *Adv. Funct. Mater.* **2009**, *19*, 3375−3380.

(35) Jin, H.; Zhao, G.; Hu, J.; Ren, Q.; Yang, K.; Wan, C.; Huang, A.; Li, P.; Feng, J. P.; Chen, J.; Zou, Z. Melittin-Containing Hybrid Peptide Hydrogels for Enhanced Photothermal Therapy of Glioblastoma. *ACS Appl. Mater. Interfaces* **2017**, *9*, 25755−25766.

(36) Huang, C.; Jin, H.; Qian, Y.; Qi, S.; Luo, H.; Luo, Q.; Zhang, Z. Hybrid Melittin Cytolytic Peptide-Driven Ultrasmall Lipid Nanoparticles Block Melanoma Growth *In Vivo*. *ACS Nano* **2013**, *7*, 5791−5800.

(37) Robertson, C. A.; Evans, D. H.; Abrahamse, H. Photodynamic Therapy (PDT): A Short Review on Cellular Mechanisms and Cancer Research Applications for PDT. *J. Photochem. Photobiol., B* **2009**, *96*, 1−8.

(38) Castano, A. P.; Demidova, T. N.; Hamblin, M. R. Mechanisms in Photodynamic Therapy: Part One-Photosensitizers, Photochemistry and Cellular Localization. *Photodiagn. Photodyn. Ther.* **2004**, *1*, 279−293.

(39) Selbo, P. K.; Weyergang, A.; Hogset, A.; Norum, O. J.; Berstad, M. B.; Vikdal, M.; Berg, K. Photochemical Internalization Provides Time- and Space-Controlled Endolysosomal Escape of Therapeutic Molecules. *J. Controlled Release* **2010**, *148*, 2−12.

(40) Dempsey, C. E. The Actions of Melittin on Membranes. *Biochim. Biophys. Acta, Rev. Biomembr.* **1990**, *1031*, 143−161.

(41) Morone, M.; Beverina, L.; Abbotto, A.; Silvestri, F.; Collini, E.; Ferrante, C.; Bozio, R.; Pagani, G. A. Enhancement of Two-Photon Absorption Cross-Section and Singlet-Oxygen Generation in Porphyrins upon Beta-Functionalization with Donor-Acceptor Substituents. *Org. Lett.* **2006**, *8*, 2719−2722.

(42) Jung, H. S.; Han, J.; Shi, H.; Koo, S.; Singh, H.; Kim, H. J.; Sessler, J. L.; Lee, J. Y.; Kim, J. H.; Kim, J. S. Overcoming the Limits of Hypoxia in Photodynamic Therapy: A Carbonic Anhydrase IX-Targeted Approach. *J. Am. Chem. Soc.* **2017**, *139*, 7595−7602.

(43) Lin, A.; Truong, B.; Patel, S.; Kaushik, N.; Choi, E. H.; Fridman, G.; Fridman, A.; Miller, V. Nanosecond-Pulsed DBD Plasma-Generated Reactive Oxygen Species Trigger Immunogenic Cell Death in A549 Lung Carcinoma Cells through Intracellular Oxidative Stress. *Int. J. Mol. Sci.* **2017**, *18*, 966−990.

(44) Krysko, D. V.; Garg, A. D.; Kaczmarek, A.; Krysko, O.; Agostinis, P.; Vandenabeele, P. Immunogenic Cell Death and DAMPs in Cancer Therapy. *Nat. Rev. Cancer* **2012**, *12*, 860−875.

(45) Maeda, H.; Wu, J.; Sawa, T.; Matsumura, Y.; Hori, K. Tumor Vascular Permeability and the EPR Effect in Macromolecular Therapeutics: A Review. *J. Controlled Release* **2000**, *65*, 271−284.

(46) Wang, Y.; Wu, Y.; Liu, Y.; Shen, J.; Lv, L.; Li, L.; Yang, L.; Zeng, J.; Wang, Y.; Zhang, L. W.; Li, Z.; Gao, M.; Chai, Z. BSA-Mediated Synthesis of Bismuth Sulfide Nanotheranostic Agents for Tumor Multimodal Imaging and Thermoradiotherapy. *Adv. Funct. Mater.* **2016**, *26*, 5335−5344.

(47) Veglia, F.; Perego, M.; Gabrilovich, D. Myeloid-Derived Suppressor Cells Coming of Age. *Nat. Immunol.* **2018**, *19*, 108−119.

(48) Gabrilovich, D. I.; Nagaraj, S. Myeloid-Derived Suppressor Cells As Regulators of the Immune System. *Nat. Rev. Immunol.* **2009**, *9*, 162−174.

(49) Ostrand-Rosenberg, S.; Sinha, P. Myeloid-Derived Suppressor Cells: Linking Inflammation and Cancer. *J. Immunol.* **2009**, *182*, 4499−4506.

(50) Chen, Z.; Liu, L.; Liang, R.; Luo, Z.; He, H.; Wu, Z.; Tian, H.; Zheng, M.; Ma, Y.; Cai, L. Bioinspired Hybrid Protein Oxygen Nanocarrier Amplified Photodynamic Therapy for Eliciting Anti-Tumor Immunity and Abscopal Effect. *ACS Nano* **2018**, *12*, 8633−8645.